The NASA/GSFC 94 GHz Airborne Solid State Cloud Radar System (CRS)

Matthew L. Walker McLinden*, Lihua Li, Gerald M. Heymsfield, Michael Coon, and Amber Emory

NASA Goddard Space Flight Center, Greenbelt, Maryland

**Corresponding author*: Matthew L. Walker McLinden, NASA/Goddard Space Flight Center, 8800 Greenbelt Rd., Greenbelt, MD 20771. matthew.l.mclinden@nasa.gov

ABSTRACT

The NASA/Goddard Space Flight Center's (GSFC's) W-band (94 GHz) Cloud Radar System (CRS) has been comprehensively updated to modern solid-state and digital technology. This W-band (94 GHz) radar flies in nadir-pointing mode on the NASA ER-2 high-altitude aircraft, providing polarimetric reflectivity and Doppler measurements of clouds and precipitation. This paper describes the design and signal processing of the upgraded CRS. It includes details on the hardware upgrades (SSPA transmitter, antenna, and digital receiver) including a new reflectarray antenna and solid-state transmitter. It also includes algorithms, including internal loop-back calibration, external calibration using a direct relationship between volume reflectivity and the range-integrated backscatter of the ocean, and a modified staggered-PRF Doppler algorithm that is highly resistant to unfolding errors. Data samples obtained by upgraded CRS through recent NASA airborne science missions are provided.

1. Introduction

Clouds play a significant role in both the global hydrological cycle and the climate through earth's radiated energy budget (Stephens et al. 1990). W-band (94 GHz) radar is a unique tool for studying cloud systems, providing higher sensitivity than lower frequency radars and better cloud penetration than lidar. The W-band spaceborne CloudSat Cloud Profiling Radar (CPR) (Stephens et al. 2002) has had great success in sampling clouds worldwide, and airborne W-band radars such as the NASA/GSFC Cloud Radar System (CRS) Li et al. (2004), the NASA/JPL Airborne Precipitation Radar 3 (APR3), and the National Center for Atmospheric Research (NCAR) HIAPER Cloud Radar (HCR) (Vivekanandan et al. 2015), compliment this capability by providing high resolution capability, multi-instrument retrievals, and targeted overpasses of atmospheric events.

The recent comprehensive upgrade of the NASA CRS instrument achieves sensitivity comparable to conventional Extended Interaction Klystron (EIK) radars with a 30-Watt Solid State Power Amplifier (SSPA) combined with an innovative 51 cm width reflectarray antenna. The use of SSPA rather than EIK technology at 94 GHz allows for highly sensitive radars with reduced mass and size, and removes the necessity of high-voltage electronics. This paper details the upgraded solid-state CRS. The hardware and performance of the instrument are shown. Additionally, algorithms are detailed, such as pulse compression with ultra-low range sidelobes, the direct relationship between volume reflectivity and normalized radar cross section, and a dual-PRF Doppler algorithm designed to minimize both the occurrence of inappropriate Doppler unfolding of high velocities and the standard deviation of the Doppler measurement. Internal and external calibration equations are discussed as well.

2. System Description

The NASA GSFC W-band (94 GHz) Cloud Radar System (CRS) was originally built in the 1990's using an extended interaction klystron (EIK) transmitter to provide cloud profiling capability to the NASA ER-2 aircraft (Li et al. 2004). The original CRS system flew in numerous field campaigns including the Cirrus Regional Study of Tropical Anvils and Cirrus Layers - Florida Area Cirrus Experiment (CRYSTAL-FACE) (Evans et al. 2005), the Tropical Composition, Cloud, and Climate Coupling (TC4) (Toon et al. 2010), the Cloudsat, Calipso Validation Experiment (CCVEX) (Mace et al. 2009), et al. Goddard Space Flight Center began a comprehensive upgrade in 2012 to modernize CRS. The use of emerging high-power W-band solid-state power amplifier (SSPA) technology improves system reliability and enables pulse compression. A new reflectarray antenna improves sensitivity and acts as a technology demo for a combined aperture W-band and Ka-band (35 GHz) spaceborne radar (Hand et al. 2013). The upgraded radar was completed in early 2014 and since then it has flown during the 2014 NASA Integrated Precipitation and Hydrology Experiment (IPHEX) (Barros et al. 2014), the 2015 NASA Radar Definition Experiment (RADEX) experiment, a NOAA 2017 GOES-R calibration/validation campaign, and the 2020 NASA Investigation of Microphysics and Precipitation for Atlantic Coast-Threatening Snowstorms (IMPACTS).

The electronic subsystems and antenna of CRS were comprehensively upgraded while maintaining the mechanical structure of the hermetic transceiver housing of the original instrument. CRS is mounted on the NASA ER-2 aircraft within the tailcone and mid-sections "superpod" payload locations as is illustrated in Fig. 1. A description of the NASA ER-2 is given by NASA/DFRC (2002). The antenna, along with a hermetic canister which houses the transceiver, waveform generator, and navigation system are located in the superpod tailcone. The RF subsystem is connected to a 0.51 m width reflectarray antenna that points nadir through an open window. The data system, digital receiver, and power distribution subsystems are located in the pressurized midbody of the aircraft superpod. The simplified system block diagram is shown in Fig. 2. CRS may also be flown in combination with the NASA Goddard Space Flight Center's High-altitude Imaging Wind and Rain Airborne Profiler (HIWRAP) radar in the left wing superpod (Li et al. 2016) using shared data system and digital receiver subsystems between the two instruments, allowing co-located Ku-, Ka-, and W-band measurements.

The upgraded CRS system takes advantage of an innovative reflectarray antenna and recent advancements in solid-state power amplifier (SSPA) technology, utilizing an SSPA and pulse compression to achieve good range resolution, sensitivity, and reliability. The performance metrics of the solid state CRS radar in its commonly deployed configuration are shown in Table 1. Descriptions of the solid-state transceiver, antenna, waveform, and digital subsystems are below.

a. Solid-State Transceiver

The CRS transceiver uses a coherent two-stage heterodyne system with the SSPA. The transmitter and receiver share the antenna with a waveguide circulator and a set of latching circulator switches to provide receiver protection. The noise figure of the receiver is set by a low-noise amplifier (LNA) and the insertion losses of front end components including a circulator, latching circulators, a mechanical waveguide switch, and waveguides. Internal calibration is achieved through a loop-back path that feeds an attenuated sample of the transmitted waveform into the receiver. This calibration subsystem is detailed in Section 4 and Appendix B.

The waveform generator creates a frequency-diversity waveform consisting of amplitude tapered pulses and an amplitude-tapered linear frequency modulated (LFM) chirp at offset frequencies centered at 60 MHz. This frequency diversity waveform is mixed in a two-stage process first to 1.9 GHz then to 94.0 GHz. The received signal is amplified by a LNA before being downconverted back to 60 MHz and digitized by the digital receiver. The heterodyne transceiver allows for flexible waveform generation and high-performance pulse compression. The total transmit bandwidth available for the frequency-diversity waveform is set to be 10 MHz with current filters, although this could be expanded up to the 40 MHz limit of the digital receiver.

The SSPA is a 30 W power-combined waveguide gallium arsenide (GaAs) amplifier designed by Quinstar Technology, Inc. shown in Fig. 3. In typical operation, the SSPA is run at 15% duty cycle. It uses an electrically controlled mute function to disable amplification during the receive time window. Compared to klystron tube-based W-band radar transmitters, the solid-state power amplifier does not require a high voltage power supply, allowing a more compact and light-weight system suitable for high-altitude operation. The SSPA can also be operated at a much higher duty cycle with long waveforms enabling pulse compression implementation.

b. Antenna

The CRS antenna was jointly developed by Goddard Space Flight Center and Northrop Grumman Mission Systems (NGMS) to demonstrate reflectarray antenna technologies for the NASA 2007 Earth Science Decadal Survey Aerosol-Cloud-Ecosystem (ACE) mission (Hand et al. 2013) under the support of a 2010 NASA Earth Science Technology Office (ESTO) Instrument Incubator Program (IIP) project. The antenna is a subscale unit to demonstrate reflector/reflectarray technology designed to share a large aperture between a horn-fed W-band radar and a line-fed Active Electronically Scanned Array (AESA) at Ka-band. The antenna reflector is mechanically a one-dimensional parabola designed to focus the Ka-band line feed for cross-track scanning. At W-band, resonators printed on the reflector surface adjust the phase of reflected electromagnetic waves to focus the beam in two dimensions, allowing the antenna to be fed by a conventional horn offset from the focus of the physical parabola. The antenna is shown in Fig. 4 during anechoic chamber testing with both the W-band horn and a Ka-band patch array line feed.

The antenna is currently used only at W-band as part of the Cloud Radar System. At W-band it has an antenna gain of 51 dB, a beamwidth of 0.45 degrees, a peak sidelobe of -27 dB, and an integrated cross polarization ratio of -28.6 dB. The antenna is designed for dual polarization using a scalar feed coupled with an orthomode transducer (OMT). The W-band antenna pattern is shown in Fig. 5. The ability of this antenna to accept a Ka-band line feed leaves open the possibility of adding dual-band capability to CRS at a future date. To avoid losses associated with a radome, the CRS antenna uses an open window protected by an air deflector in the aft section of the superpod tailcone as shown in Fig. 1c.

c. Waveform

CRS employs both pulse compression and frequency diversity in its waveform. Pulse compression is used to improve the sensitivity compared to conventional pulsed continuous-wave (CW) waveforms. Frequency diversity allows multiple waveforms to be transmitted and received in each pulse repetition interval (PRI) by transmitting and receiving them at slightly offset frequencies.

The pulse compression technique is to use a chirp or other broadband signal to decouple a waveform's bandwidth from its length, allowing additional transmitted energy for a given bandwidth. This can substantially improve radar sensitivity. Two drawbacks of pulse compression waveforms are the presence of a blind range near the radar and range sidelobes from strong reflectors such as the Earth's surface. The selection of a pulse compression waveform is a trade on radar sensitivity, range resolution, pulse compression sidelobes, and blind range.

The blind range of a pulse compression waveform depends on the length (or time) of the chirp, and is due to the radar's inability to receive weak signals while transmitting. The pulse compression sidelobes additionally may mask small signals near strong reflectors if the sidelobe level is comparable to the radar sensitivity. Generally, pulse compression sidelobes can be reduced by increasing the time-bandwidth product of a chirp. Increasing the chirp length increases the blind range, and may also increase the spread of possible sidelobes. Increasing the chirp bandwidth improves range resolution but degrades sensitivity for volume targets. Amplitude tapering on transmit can also improve sidelobe performance (at the expense of sensitivity and range resolution), but complex amplitude tapers require the transmitter to be run outside of saturation, further degrading sensitivity.

The length of the CRS chirp was selected as 30 μs, corresponding with a blind range of approximately 5 km. This allows use of the LFM chirp at heights up to 15 km above the surface at the nominal ER-2 flight altitude of 20 km. The chirp bandwidth is set to 3 MHz. The chirp produced by the waveform generator has a Hann taper in amplitude, however the transmitter is driven to saturation, resulting in an amplitude tapered waveform more similar to a Tukey window. The receive filter is a matched filter of the saturated chirp with an additional Hann window applied in time domain. The relative amplitude of the chirp before and after transmitter saturation is shown in Fig. 6.

The pulse compressed chirp has a range resolution of 115 meters at 6 dB taper. The pulse compression sidelobes measured through internal calibration and laboratory testing are -70 dB at 600 meters from the peak of the compressed pulse, however realized sidelobes from exceptionally strong surface targets show that pulse compression performance is somewhat worse, reaching -60 dB by 700 meters. The sidelobes from exceptionally strong surface returns do not share the Doppler signature of the surface, but rather have a uniformly distributed random phase after Doppler processing. The cause of the difference between loopback and surface range sidelobes is not fully understood at this time but is consistent with system phase noise.

The pulse compression sidelobes are shown in Fig. 7. The tapered 30 μs 3 MHz pulse compression chirp has an effective pulse length of 18 μs, a -6 dB range weighting function (after pulse compression) of 0.77 μs (115 meters), and a noise bandwidth of 1.1 MHz, for a pulse compression gain of 13.7 dB. Pulse compression performance metrics are discussed in more detail in Section 3a.

While pulse compression is used for most radar ranges, CRS utilizes a frequency-diversity waveform to provide two conventional single-tone pulses for use if pulse compression data is not available due to the chirp blind range or range sidelobes. The two single tone pulses and LFM chirp are transmitted in succession at slightly offset frequencies (subchannels) during every PRI. The frequency offsets allow the digital receiver to separate and receive the echoes of the single tone pulses and chirp simultaneously.

The first subchannel is a 2.5 μs single-tone pulse with amplitude tapering using a raised cosine window. This performs somewhat similarly to a 1.5 μs conventional pulse however it is more contained in the frequency domain. While the SSPA is run in saturation and thus reduces the the amplitude tapering, this tapering is important to reduces crosstalk between subchannels. The second subchannel is the 30 μs 3 MHz LFM chirp with amplitude tapering previously described. The third subchannel is a single tone pulse similar to the first one but at a different center frequency. The center frequencies are separated by 5 MHz (adjustable). An illustration of the frequency diversity waveform is shown in Fig. 8.

This pulse-chirp-pulse waveform strategy is detailed by McLinden et al. (2013). The chirp is used in radar ranges from 5 km below the aircraft to approximately 1 km above the surface for improved sensitivity. The second single-tone pulse, transmitted last, may experiences a blind range of less than 1 km and provides data coverage in the chirp blind range due to channel-channel crosstalk. Within 1 km of the surface the chirp channel may experience surface echo range sidelobes that obfuscate the weather signal. In this case data from the first single-tone pulse may be used to cover the near-surface range. Two pulses are used rather than one so as to limit the presence of crosstalk between the channels due to the very strong surface echo. Approximate sensitivity as a function of range and height is shown in Figure 9. In the most recent IMPACTS 2020 dataset only the chirped data is used by default.

d. Digital Subsystems

The waveform generator uses a Xilinx Spartan 6 field programmable gate array (FPGA) and a Texas Instruments digital-to-analog converter (DAC). The waveform generator provides all switch timing signals to the transmitter, receiver protection switches, and digital receiver. It stores an arbitrary waveform onboard in the FPGA block ram that allows for fully customizable waveforms at 80 megasamples per second (MSPS). The second Nyquist zone of the DAC (40-80 MHz) is used to produce 40 μs frequency diversity waveforms in an IF frequency of 50 to 70 MHz.

The waveform generator also controls switch timing for the transceiver. TTL logic is used to trigger the SSPA, latching circulator switches, and digital receiver. Transmission is enabled by a TTL signal from the CRS datasystem, which is passed through an aircraft interlock to allow pilot control of transmission. An additional altitude switch is used to prevent transmission on the ground, protecting the system from accidental triggering.

The CRS uses a high-speed digital receiver and signal processor developed by Remote Sensing Solutions (RSS) for the High-Altitude Wind and Rain Atmospheric Profiler (HIWRAP) radar (Li et al. 2016). The digital receiver can accept up to four receiver cards, however when flying alone CRS uses only a single card, adequate for co-pol and cross-pol channels. Each receiver card uses Xilinx Virtex 5 FPGAs combined with two 160 MSPS 14-bit A/D converter channels. The receiver splits signals from the two A/Ds into as many as eight digitally downconverted subchannels. For

CRS, one A/D is used for the co-polarization receiver and the other is used for the cross-polarization receiver. Each subchannel has digital downconversion (can be tuned to a desired center frequency using numerical controlled oscillators), matched filtering, and pulse-pair processing (power, dual-PRF first lag, and second lag). The subchannels have customizable bandwidths ranging from 500 kHz to 20 MHz, with an aggregate bandwidth of 40 MHz. The bandwidth individual subchannels must be 40/N MHz where N is an integer. Subchannels can also operate in a raw data mode that outputs the complex digitally downconverted data without onboard processing such as pulse pair or pulse compression. The output data from the digital receiver is sent to the data system over gigabit Ethernet, and will typically range from 10 MBPS to 80 MBPS depending on radar configuration.

The CRS digital receiver is typically configured to use six 5.71 MHz bandwidth subchannels with both ADCs for pulse-pair processing. Three subchannels are used to receive the co-polarization returns from the frequency diversity waveform. An additional three channels are used to receive the cross-polarization returns. For IMPACTS, an additional subchannel was used to record raw data for the co-polarization chirp.

The data system is a commercial single board computer (SBC) with a Linux operating system. The SBC runs a radar control program that automates the radar configuration and operation based on command inputs provided by the pilot. The radar control program interfaces with a commercial off-the-shelf (COTS) Compact PCI multi-function I/O card that controls power to radar subsystems, enables transmit, and inputs telemetry and fault status. The data system receives data from the digital receiver subsystem over gigabit ethernet and records it to disk. It also receives navigation data from the dedicated navigation system over RS232 or ethernet and from the aircraft navigation system over ethernet. The SBC transmits a small portion of received data to the ground in real-time to provide feedback to mission scientists and engineers as to the quality of data and the structure of the clouds and precipitation.

3. Measurement Products

The standard measurement products produced by CRS are volume reflectivity, linear depolarization ratio (LDR), Doppler velocity and spectrum width, and surface normalized radar cross section (NRCS). An example of reflectivity, LDR, Doppler velocity, and spectrum width are shown in Fig. 10, and are described in detail below. The algorithm for volume reflectivity is discussed in detail to show the impact of pulse compression on sensitivity, bandwidth, and calibration. The dual-PRF Doppler velocity algorithm has been modified to achieve low standard-deviation velocity measurements with minimal unfolding errors. The NRCS algorithm (derived in the Appendix) is in a range-integrated form that allows a direct relationship of the beam-limited NRCS with volume reflectivity, independent of pulse length or actual beam-filling.

a. Volume Reflectivity

The radar equation for clouds or precipitation is expressed as (Doviak and Zrnić 2006)

$$P_\eta(r) = \frac{P_t g_s g^2 \lambda^2 \eta(r)}{(4\pi)^3 r^2 l_{\text{atm}}^2(r) l_{\text{tx}} l_{\text{rx}} l_{\text{rad}}^2} \int |W_s(r')|^2 dr' \iint f^4(\theta', \phi') \sin\theta' \partial\theta' \partial\phi' \tag{1}$$

where $P_\eta(r)$ is the received signal power referred to the receiver output in watts, P_t is the peak transmit power in watts, g_s is the receiver gain, λ is the radar signal wavelength in meters, η is the volume reflectivity in m^2m^{-3}, r is range in meters, l_{atm} is the atmospheric attenuation, l_{tx} is the transmitter loss, l_{rx} is the receiver loss, l_{rad} is the radome loss, g is the antenna gain, and $f^4(\theta, \phi)$ is the unitless two-way antenna function normalized to a maximum of one at polar coordinates θ and ϕ in radians, and $\int |W_s(r')|^2 dr'$ is the range weighting function integral in meters. The range weighting function W_s is the unitless convolution of the transmitted wave envelope e normalized to a peak of 1 and the receiver impulse response h normalized to a gain of 1. This equation assumes that the volume reflectivity and r^2 is constant within the range cell volume illuminated by the radar.

The range weighting function integral for pulsed channels is typically represented as

$$\int_{r'} |W_s(r')|^2 dr' = \frac{c\tau_{\text{eff}}}{2l_r} \tag{2}$$

where the effective pulse length τ_{eff} in seconds is

$$\tau_{\text{eff}} = \int_{t'} |e(t')|^2 dt', \tag{3}$$

$e(t)$ is the transmitted wave envelope, and the finite bandwidth loss l_r is

$$l_r = \frac{\int_{t'} |e(t')|^2 dt'}{\int_{t'} |e(t') * h(t')|^2 dt'}. \tag{4}$$

The receiver impulse response is $h(t)$. For a linear receiver, $h(t)$ is the digital pulse compression filter.

For the pulse compressed channel the range weighting function integral is

$$\int_{r'} |W_s(r')|^2 dr' = \frac{c\tau_{6\text{dB}} g_{\text{pc}}}{2} \tag{5}$$

where $\tau_{6\text{dB}}$ is the effective pulse width in seconds associated with the 6 dB range resolution of the compressed chirp and the pulse compression gain g_{pc} is

$$g_{\text{pc}} = \frac{\int_{t'} |e(t') * h(t')|^2 dt'}{\tau_{6\text{dB}}}. \tag{6}$$

Note that the underlying equations are identical for the pulsed and chirp channels, with the only difference being housekeeping of the finite bandwidth loss and the pulse compression gain.

These terms are insufficient to determine radar sensitivity with a pulse compression radar, as the noise bandwidth B in s^{-1} is not $1/\tau$ for shaped and compressed waveforms. The bandwidth must be calculated directly from the receiver impulse response,

$$B = \frac{\int_{t'} |h(t')|^2 dt'}{\left|\int_{t'} h(t') dt'\right|^2}. \tag{7}$$

The volume reflectivity η is converted to the equivalent reflectivity factor in mm^{6}m^{-3} according to the relationship

$$Z_e = \frac{\eta \lambda^4 10^{18}}{\pi^5 |K_w|^2}, \tag{8}$$

where $|K_w|^2$ is 0.75 (for water at 10$^\text{o}$ C) by convention at W-band (Stephens et al. 2008).

Analysis of the expected value and standard deviation of the reflectivity measurement follows Doviak and Zrnić (2006) (errata) and Fukao et al. (2014). The power received by the radar is the square of the summed volume reflectivity signal and noise signals. The estimated volume reflectivity power $\hat{P}_\eta$ is the averaged received power including noise N with the estimated mean noise power $\hat{\bar{N}}$ subtracted. The expected value of the estimated reflectivity power is the sum of expected value of the mean reflectivity power $\bar{P}_\eta$ and the difference of the expected values of the mean noise power $\bar{N}$ and the estimated mean noise, as

$$\mathrm{E}(\hat{P}_\eta) = E(\bar{P}_\eta) + E(\bar{N}) - \mathrm{E}(\hat{\bar{N}}). \tag{9}$$

The mean noise power for CRS is estimated to very good accuracy and precision with a recursive algorithm. The median profile power provides an initial estimate of the mean power, and all range gates greater than three standard deviations above the mean (according to theory based on the number of averaged profiles) are removed. This process is repeated until all data falls within three standard deviations of the estimated median. The estimated noise for each profile is then put through a running-median filter. This process removes to a great extent any reflectivity signal from the estimated noise without requiring a priori knowledge of range gates clear of reflectivity targets. The result is that the standard deviation and offset of the estimated mean noise are both substantially smaller than the standard deviation of the noise ($\mathrm{std}(\hat{\bar{N}}) \ll \mathrm{std}(\bar{N})$ and $|\hat{\bar{N}} - \bar{N}| \ll \mathrm{std}(\bar{N})$) even in data with substantial clouds and precipitation.

After thresholding described below, the expected value of the estimated volume reflectivity signal power is approximately equal to the mean of the actual reflectivity signal power $\bar{P}_\eta$,

$$\mathrm{E}(\hat{P}_\eta) \approx \bar{P}_\eta, \tag{10}$$

and the standard deviation of the estimated volume reflectivity signal power is approximately the standard deviation of the summed volume reflectivity power and noise divided by the number of independent samples M_I,

$$\mathrm{std}(\hat{P}_\eta) \approx \frac{\bar{P}_\eta + \bar{N}}{\sqrt{M_I}}. \tag{11}$$

The number of independent samples includes the effects of both the spectrum width of the target and the thermal noise.

The standard deviation of the power received from single backscattered pulse from randomly distributed scatterers and the thermal noise is equal to the mean combined power for a square-law receiver such as is used in the the digital processor for CRS. The standard deviation of the measurement is decreased by averaging M pulses. The thermal noise in each pulse is uncorrelated. The backscatter from volume targets are correlated from pulse to pulse, depending on the velocity spectrum including the impact of forward aircraft motion due to the beamwidth of the antenna. The number of independent samples for the volume backscatter (without including thermal noise) is approximated by

$$M_i \approx \frac{4\sqrt{\pi} M T \sigma_v}{\lambda} \tag{12}$$

where M is the number of averaged pulses, T is the pulse repetition time in seconds, σ_v is the target spectrum width in ms^{-1}. This assumes the $M \gg 1$ and $2T\sigma_v/\lambda \ll 1$.

As shown in Doviak and Zrnić (2006) (errata) and Fukao et al. (2014), the number of independent samples M_I including both the thermal noise and the volume scatterer velocity spectrum is estimated with reasonable assumptions by

$$M_I \approx M \frac{(1+\mathrm{SNR})^2}{1+2\,\mathrm{SNR}+\mathrm{SNR}^2 \frac{M}{M_i}} \tag{13}$$

where M is the number of averaged pulses and M_i is the number of independent samples of reflectivity based on the velocity spectrum width given in Eq. (12), and SNR is the unitless signal-to-noise ratio.

The ratio of the standard deviation of the reflectivity measurement to the mean reflectivity is then a function of both the spectrum width of the target and the signal-to-noise ratio (SNR) of the received signal power P_η,

$$\frac{\mathrm{std}(\hat{P}_\eta)}{\bar{P}_\eta} \approx \sqrt{\frac{1}{M_i} + \frac{2}{\mathrm{SNR}\,M} + \frac{1}{\mathrm{SNR}^2\,M}} \tag{14}$$

where $\mathrm{std}(\hat{P}_\eta)$ is the standard deviation of the estimated received signal power in Watts (after mean noise subtraction) and $\bar{P}_\eta$ is the mean received power (without noise). This shows that for high SNR the uncertainty will typically be dominated by the number of independent reflectivity samples, but for low SNR the uncertainty will be dominated by the residual noise after mean-noise subtraction and the total number of averaged pulses.

Radar reflectivity measurement sensitivity is typically specified at the signal to noise ratio threshold equal to the first standard deviation (1-sigma) of the thermal noise, or SNR = $1/\sqrt{M}$, where all signals below this power will be ignored. From Eq. (14), this will correspond to approximately a 100% standard deviation (in linear units) for a reflectivity measurement at the sensitivity threshold. Sensitivity of CRS with respect to reflecitivity and signal-to-noise ratio is shown in Fig. 11 assuming a spectrum width of 1 m/s and a sensitivity of -30 dBZe.

b. Linear Depolarization Ratio

CRS incorporated a cross-polarization receive channel starting with the NASA 2015 Radar Definition Experiment (RADEX), allowing Linear Depolarization Ratio (LDR) measurements. The algorithm used is (Bringi and Chandrasekar 2001)

$$\mathrm{LDR} = 10\log_{10}\frac{\hat{P}_{\mathrm{cross}}}{\hat{P}_{\mathrm{co}}}, \tag{15}$$

where $\hat{P}_{\mathrm{co}}$ is the estimated power in watts of the received signal in the co-polarized channel and $\hat{P}_{\mathrm{cross}}$ is the estimated power in watts of the received signal in the cross-polarized channel. The LDR signal is thresholded similarly to the reflectivity factor, being primarily limited by the signal-to-noise ratio of the cross-polarization channel.

c. Doppler Velocity

CRS uses dual-PRF Doppler processing with a staggered 5/4 ratio pulse repetition frequency (PRF) to increase the unambiguous velocity. The pulse repetition intervals (PRIs) of 224 μs and 280 μs provide an unambiguous velocity of 14.25 m/s. From Holleman and Beekhuis (2003), Dual-PRF processing has the drawback of increased measurement standard deviation, 6.4 times that of the single-PRF standard deviation. The dual-PRF velocity estimate can be used to unfold the single-PRF estimate, but errors in this unfolding may be problematic.

Published dual-PRF dealiasing algorithms such as Joe and May (2003) and Torres et al. (2004) use the dual-PRF velocity estimate to calculate the number of times the single-PRF velocities are aliased based on a set of rules to estimate the Nyquist interval of the single-PRF velocity. These methods lead to the presence of many edge cases, where the dual-PRF velocity estimate falls near a single PRF Nyquist velocity. In these edge cases, even a small error in the initial dual-PRF velocity estimate may cause incorrect dealiasing. For CRS use an algorithm that does not calculate the single-PRF Nyquist intervals but instead shifts the single-PRF Nyquist interval to be centered on an initial dual-PRF velocity estimate, maximizing the resistance of the algorithm to folding errors.

The CRS Doppler algorithm begins with an initial dual-PRF Doppler velocity estimate using the difference in phase between the high- and low-PRF lag-one autocovariance phasors (Doviak and Zrnić 2006). Expressed only in terms of velocity estimates as in Holleman and Beekhuis (2003), the initial dual-PRF velocity estimate is

$$\hat{v}_{hl} = (5\hat{v}_l - 4\hat{v}_h)\,|_{\pm v^u_{hl}} \tag{16}$$

where $\hat{v}_l$ is the low-PRF velocity estimate in m/s, $\hat{v}_h$ is the high-PRF velocity estimate in m/s. The $\pm v^u_{hl}$ term indicates that the result is wrapped around the dual-PRF unambiguous velocity and the notation $x\,|_{\pm y}$ is used to indicate $((x+y)$ modulo $2y)-y$. This initial estimate has increased unambiguous velocity at the cost of significantly increased standard deviation.

The single-PRF measurements are used to refine the initial dual-PRF estimated velocity. First, the dual-PRF estimated velocity is subtracted from the single-PRF estimated velocity. The residual single-PRF velocity provides a velocity delta that indicates the difference between the dual-PRF velocity estimate and a perfectly unfolded single-PRF velocity estimate. The single-PRF velocity delta is

$$\Delta v_{h/l} = \left(\hat{v}_{h/l} - \hat{v}_{hl}\right)|_{\pm v^u_{h/l}} \tag{17}$$

where $\hat{v}_{h/l}$ is the single high or low PRF velocity estimate and $v^u_{h/l}$ is the unambiguous velocity for the high or low PRF.

Unfolded single-PRF velocity estimates are made by adding the delta velocity $\Delta v_{h/l}$ to the initial dual-PRF velocity estimate from Eq. (16). This has the practical effect of centering the single-PRF unambiguous velocity around the initial dual-PRF estimate, ensuring the largest error tolerance before folding errors corrupt the estimate. This algorithm is resistant to velocity errors in Eq. (16) smaller than the single-PRF unambiguous velocities.

Assuming no unfolding errors, the resulting estimate is exactly equal to a perfectly unfolded single-PRF velocity. To minimize the standard deviation of the measurement, the velocity delta estimates from both the high- and low-PRF are averaged to create the final velocity estimate $\hat{v}$ as

$$\hat{v} = \hat{v}_{hl} + \left(\frac{1}{2}\Delta v_h + \frac{1}{2}\Delta v_l\right). \tag{18}$$

Variance of the velocity estimate could be slightly decreased by performing a weighted average of Δv_h and Δv_l based on the theoretical standard deviation of pulse-pair velocities associated with the PRFs rather than equal weighting, however that is not currently implemented with CRS data. Alternatively, the smaller magnitude of Δv_h or Δv_l could be used for a slight increase in resistance to unfolding interval errors at the cost of increased standard deviation. This unfolding algorithm is illustrated in Fig. 12.

The algorithm is resistant to aliasing errors so long as errors in the the initial estimate from Eq. (16) are moderately less than the single-PRF Nyquist velocity. This depends on the spectral width of the target and the signal to noise ratio. Occasional residual Doppler aliasing errors may occur even with high SNR in areas with very high spectral width, such as range gates including both precipitation and the Earth surface (resulting in a bimodal velocity spectrum larger than the single-PRF spectrum width). An example of Doppler data is shown in Fig. 13. As expected, the CRS dual-PRF Doppler algorithm is visibly less noisy than that using Eq. (16), and shows no speckle associated with decision-tree dealiasing algorithms. The data shows the algorithm to be nearly 100% resistant to Doppler velocity aliasing errors when the signal to noise ratio is better than -7 dB with rain and cloud targets and 1830 averaged pulses. This algorithm was used to produce the velocity data shown in Fig. 10c.

Doppler velocity error is caused by phase noise, velocity spectrum width, non-uniform beam filling (NUBF), aircraft motion, and the intrusion of horizontal winds into the vertical measurement due to off-nadir pointing. The aircraft motion and horizontal winds are the dominant sources of error. Aircraft motion is subtracted from the Doppler measurement based on data from an inertial measurement unit (IMU) contained within the transceiver. The standard deviation of the measured Doppler velocity of the ocean is less than 0.15 m/s after aircraft motion subtraction. As the radar beam is pointing near nadir, the ocean should have a radial velocity of 0 m/s. This gives the combined uncertainty of Doppler velocity measurements due to systematic effects and aircraft motion. The effect of horizontal winds depends on the off-nadir angle of the beam (a function of the aircraft attitude) and the velocity of the horizontal winds. This can be estimated based on radar navigation data and modeled or measured horizontal winds, however that processing is not currently included in CRS data products.

d. Spectrum Width

The Doppler velocity spectrum width (shown in Fig. 10d) is estimated using the square root of the log of the ratio of the zero- and first moment data as described in Doviak and Zrnić (2006). This equation is

$$\sigma_v = \frac{\lambda}{2\pi\sqrt{T_{s1}^2 - T_{s0}^2}}\sqrt{\ln\left|\frac{\hat{R}_0}{\hat{R}_1}\right|} \tag{19}$$

where $\hat{R}_0$ and $\hat{R}_1$ are the pulse-pair autocorrelations at lag-0 and lag-1 with the mean noise subtracted from the lag-0, and T_{s0} and T_{s1} are the pulse-pair intervals (0 μs and 224 or 280 μs, staggered). The spectral width is calculated separately for the staggered high- and low-PRF, and the results are averaged. The fast movement of the ER-2 aircraft combined with the beamwidth of the antenna causes a minimum spectral width of approximately 1 m/s in observed data.

e. Normalized Surface Radar Cross Section

The use of a range-integrated measurement rather than the peak or an interpolated surface measurement allows the surface normalized radar cross section to be retrieved without requiring corrections for the complex interaction of the range weighting function, antenna pattern, and sample spacing, one approximation of which is derived by Kozu (1995). Additionally, it removes error due to instances where the 'peak' of the return is not centered on a range gate (Caylor et al. 1997; Tanelli et al. 2008). This technique requires that the range weighting function be at least approximately Nyquist sampled by the range gate spacing (McLinden et al. 2015), a technique sometimes referred to as "oversampling."

The normalized surface radar cross section is calculated using the relationship (derived in Appendix A),

$$\sigma^0 = \sum \eta_s[r] \Delta r \cos\phi_0. \tag{20}$$

where η_s is the measured volume reflectivity due to the surface backscatter, Δr is the range gate spacing in meters, $\cos\phi_0$ is the off-nadir angle factor. This equation provides the normalized surface radar cross section over the full surface illuminated by the two-way antenna pattern. It assumes that the normalized radar cross section is constant over the illuminated surface,

$$\frac{\sigma^0(\theta', \phi')}{\cos\phi' \sin\theta'} \approx \frac{\sigma^0(\phi_0)}{\cos\phi_0}, \tag{21}$$

and that the range-squared and atmospheric loss are constant over the range weighting function. For this application the measured volume reflectivity from the surface is summed over 15 range gates (approximately 400 m) centered on the estimated range to the ocean surface based on aircraft navigation data.

4. Calibration

CRS data is calibrated using backscatter from the ocean surface (Li et al. 2005). As many flights do not allow calibration maneuvers over the ocean and as system performance will drift with temperature, absolute calibration is maintained for individual field campaigns through an internal calibration loop that feeds a small portion of the transmitted waveform into the receiver. The internal calibration loop has been used by new generation weather radars such as the University of Massachusetts Advanced Multi-Frequency Radar (AMFR) (Majurec et al. 2004), the NASA/Goddard Space Flight Center (NASA/GSFC) High Altitude Wind and Rain Airborne Profiler (HIWRAP) (Li et al. 2016), the Cloud Radar System (CRS), and the ER-2 X-band Radar (EXRAD) instruments. Variants have been used in other instruments such as the NASA/Goddard EcoSAR radar (Rincon et al. 2015) as well. A simplified schematic of the CRS calibration loop is shown in Fig. 14.

CRS uses a range-integrated calibration method for both internal and external calibration that removes the need to estimate the finite bandwidth loss and pulse compression gain of the instrument. This simplifies the calibration of the instrument by removing the need to separately measure and book-keep these parameters for each subchannel in the frequency diversity waveform. A power detector and noise diode also provide a way to track transmit power and receiver gain independently.

The internal calibration exists to provide stability between external calibration maneuvers. For CRS, a mechanical waveguide switch redirects the input of the LNA from the receiver protection switch network to a separate loopback path that couples a small portion of the transmitted signal at the output of the SSPA. A mechanical switch was chosen to minimize loss and reduce cost compared to latching circulators, however this approach requires that calibration must be done on an intermittent basis rather than on a per-pulse basis. The calibration mode is controlled automatically by the data system computer or manually by external network control.

For the IMPACTS 2020 field campaign, CRS was externally calibrated with roll maneuvers over the ocean three times. Calibration was performed at 8 degrees off nadir (for resistance to the effects of wind on surface NRCS) with atmospheric attenuation correction from nearby soundings. Calibrated sensitivity of -30 dBZe with one-sigma noise thresholding at 10 km differs by one dB from a -31 dBZe estimate provided by a system link budget analysis of internal components. These results provide confidence that final calibration was within the 2 dB accuracy required for IMPACTS.

Specific internal and external calibration algorithms are derived in Appendix B.

5. Conclusions and Future Work

The upgraded solid-state CRS is a dual-polarization solid-state radar utilizing pulse compression, frequency diversity, and a staggered PRF. CRS serves the atmospheric community by providing cloud and light precipitation data from a high-altitude platform in conjunction with a host of other remote sensing instruments on the ER-2. Since its upgrade, CRS has participated in several experiments including IPHEX (2014), RADEX (2015), GOES-R calibraiton/validation (2017), and IMPACTS (2020). During this time the instrument has been refined with improved algorithms and pulse compression performance.

As a SSPA-based airborne cloud radar with 30 Watts of peak transmit power, CRS is also a platform for testing and demonstrating algorithms and hardware in a high-altitude space-like environment. The CRS transmitter is built with GaAs technology. As SSPA power and efficiency continues to increase with GaN technology, the algorithms and principles used in the development of CRS will also increase in importance. Solid-state cloud radars are likely to decrease in size and cost, enabling more and lower cost measurements compared to older klystron-based systems.

Future work on CRS includes efforts to further improve the pulse compression range sidelobes as well upgrading the transceiver hardware to incorporate a new 50 Watt solid-state transmitter also developed by QuinStar through NASA Small Business Innovation Research (SBIR) funding support spaceborne technology demonstration.

Acknowledgments. This work resulted from various funding sources including the NASA ACE Decadal Mission, NASA/Goddard Space Flight Center internal resources, and by the NASA Earth Science Technology Office (ESTO). The IMPACTS project was funded by the NASA Earth Venture Suborbital-3 (EVS-3) program and data are publicly available at the NASA GHRC.

Data availability statement. The data shown in Fig. 10 are from the IMPACTS science flight Level 1B data for January 25, 2020. Dataset available online from the NASA EOSDIS Global Hydrology Resource Center Distributed Active Archive Center, Huntsville, Alabama, U.S.A. doi: http://dx.doi.org/10.5067/IMPACTS/CRS/DATA101.

Data shown in Fig. 13 are from the NOAA GOES-R calibration/validation campaign Level 0 data from April 11, 2017, and can be obtained at http://har.gsfc.nasa.gov.

APPENDIX A

Derivation of the direct relationship between the beam-limited normalized radar cross section and volume reflectivity for arbitrary pulse lengths

The scatterometer radar equation relates the received power to the unitless normalized radar cross section $\sigma^0(\phi)$ that is the radar cross section of the surface per unit surface area at off-nadir angle ϕ. The radar equation for a surface target integrates the normalized radar cross section over the illuminated area as (Kozu 1995).

$$P_s = \frac{P_t g_s g^2 \lambda^2}{(4\pi)^3 l_{\mathrm{tx}} l_{\mathrm{rx}} l_{\mathrm{rad}}^2} \iint_S \frac{\sigma^0(S') f^4(S')}{R^4(S') l_{\mathrm{atm}}^2(S')} dS' \tag{A1}$$

where P_t is the transmitter power, g_s is the receiver gain, λ is the wavelength, l_{tx} is the transmitter loss, l_{rx} is the receiver loss, l_{rad} is the radome loss (if applicable), S is the integrated surface in m^2, $\sigma^0(S')$ is the normalized radar cross section of each point on the surface, g is the antenna gain, f^4 is the normalized two-way antenna pattern at each point on the surface, R is the range in meters to each point on the surface, and l_{atm} is the atmospheric loss to each point on the surface.

For a semi-pulse limited case it is necessary to include the range weighting function, as the surface will be illuminated differently at different radar range-times r. The radar equation including the range weighting function is

$$P_s(r) = \frac{P_t g_s g^2 \lambda^2}{(4\pi)^3 l_{\mathrm{tx}} l_{\mathrm{rx}} l_{\mathrm{rad}}^2} \iint_S \frac{\sigma^0 f^4 |W_s(R-r)|^2}{R^4 l_{\mathrm{atm}}^2} dS'. \tag{A2}$$

where r is the radar range-time and $|W_s(R-r)|^2$ is the range weighting function.

To link the surface integral to the natural spherical coordinates of the radar, this derivation defines nadir as lying at the polar coordinate equator ($\theta = \pi/2$) and polar coordinate azimuth $\phi = 0$. Any rotation of the antenna off-nadir is assumed to be performed in the coordinate azimuthal ϕ dimension. Note that the polar coordinates used in this appendix are not the same as those commonly used with respect to the horizon, but is instead rotated 90 degrees to simplify the derivation. The natural coordinate of the surface is considered to be cartesian with the radar at the origin. The surface can be considered a plane on the y and z dimensions lying at $x = H$ where H is the altitude in meters of the radar. An illustration of the coordinate system is shown in Fig. A1.

With these coordinate definitions, the range r to any point on the surface can be written in terms of the radar height and spherical coordinate angles as

$$r(S') = \frac{H}{\sin(\theta(S'))\cos(\phi(S'))}. \tag{A3}$$

The y coordinate in meters of the surface plane can be written as

$$y = r\sin\phi\sin\theta = \frac{H\sin\phi}{\cos\phi} \tag{A4}$$

and the z coordinate in meters of the surface plane can be written as

$$z = r\cos\theta = \frac{H\cos\theta}{\sin\theta\cos\phi}. \tag{A5}$$

The surface integral can then be converted to θ and ϕ coordinates as

$$P_s(r) = \frac{P_t g_s g^2 \lambda^2}{(4\pi)^3 l_{\text{tx}} l_{\text{rx}} l_{\text{rad}}^2} \iint \frac{\sigma^0 f^4 |W_s(R-r)|^2 H^2}{R^4 l_{\text{atm}}^2 \cos^3\phi' \sin^3\theta'} \sin\theta' \partial\theta' \partial\phi'. \tag{A6}$$

Removing the height term in favor of range gives,

$$P_s(r) = \frac{P_t g_s g^2 \lambda^2}{(4\pi)^3 l_{\text{tx}} l_{\text{rx}} l_{\text{rad}}^2} \iint \frac{\sigma^0}{\cos\phi' \sin\theta'} \frac{f^4 |W_s(R-r)|^2}{R^2 l_{\text{atm}}^2} \sin\theta' \partial\theta' \partial\phi'. \tag{A7}$$

The customary approximations for surface scatterometry can then be applied. First, the antenna pattern is assumed to be narrow enough such that the normalized radar cross section is constant around the off-nadir pointing angle of the antenna,

$$\frac{\sigma^0(\theta', \phi')}{\cos\phi' \sin\theta'} \approx \frac{\sigma^0(\phi_0)}{\cos\phi_0} \tag{A8}$$

where ϕ_0 is the nominal pointing angle off-nadir of the radar beam. The $\sin\theta'$ term is removed as the narrow beam is assumed to be centered at $\theta = \pi/2$ so $\sin\theta' \approx 1$. The atmospheric loss and range-squared terms are also assumed to be constant over the ranges illuminated by the range weighting function ($R^2(\theta', \phi') \approx r^2$ and $l_{\text{atm}}^2(\theta', \phi') \approx l_{\text{atm}}^2(r)$). This leaves

$$P_s(r) = \frac{P_t g_s g^2 \lambda^2 \sigma^0(\phi_0)}{(4\pi)^3 l_{\text{tx}} l_{\text{rx}} l_{\text{rad}}^2 l_{\text{atm}}^2(r) r^2 \cos\phi_0} \iint f^4 |W_s(R-r)|^2 \sin\theta' \partial\theta' \partial\phi'. \tag{A9}$$

Integrating over range allows the range weighting function to be pulled out of the integral as

$$\int_r P_s(r) r^2 l_{\text{atm}}^2(r) dr = \frac{P_t g_s g^2 \lambda^2 \sigma^0(\phi_0) \int |W_s(r')|^2 dr'}{(4\pi)^3 l_{\text{tx}} l_{\text{rx}} l_{\text{rad}}^2 \cos\phi_0} \iint f^4 \sin\theta' \partial\theta' \partial\phi'. \tag{A10}$$

The antenna pattern is often approximated for scatterometry as being the maximum gain G_A within the 3 dB beamwidth and zero outside, as

$$\iint f^4 \sin\theta' \partial\theta' \partial\phi' \approx \frac{\pi \Phi_{3\text{dB}}^2}{4}. \tag{A11}$$

This approximation is recognized as having up to 2 dB error (Long 2001). The approximation of the integrated antenna pattern can be improved using direct antenna pattern measurements or the Gaussian antenna approximation (Probert-Jones 1962),

$$\iint f^4 \sin\theta' \partial\theta' \partial\phi' \approx \frac{\pi \Phi_{3\text{dB}}^2}{8 \ln 2}. \tag{A12}$$

The range weighting function integral is often approximated using the combination of an idealized boxcar-shaped pulse and a “finite bandwidth loss" factor (Doviak and Zrnić 2006),

$$\int |W_s(r')|^2 dr' \approx \frac{c\tau}{2 l_r} \tag{A13}$$

where c is the speed of light in m/s, τ is the pulse length in seconds, and l_r is the finite bandwidth loss.

With both the range weighting function integral and the antenna integral, Eq. (A10) can be inverted to provide an estimate of surface normalized backscatter given an integrated received power (using discrete range gates) and radar parameters as

$$\sigma^0 = \frac{(4\pi)^3 l_{\text{tx}} l_{\text{rx}} l_{\text{rad}}^2 \left(\sum P_s[r] r^2 l_{\text{atm}}^2[r] \Delta r\right) \cos\phi_0}{P_t g_s g^2 \lambda^2 \int |W_s(r')|^2 dr' \iint f^4 \sin\theta' \partial\theta' \partial\phi'}. \tag{A14}$$

The received power P_s in Eq. (A14) assumes that the target is the surface. The received power P_η in Eq. (1) assumes that the target is a volume reflectivity. By substituting P_η from Eq. (1)

in place of P_s in Eq. (A14) we achieve a relationship between the apparent calibrated volume reflectivity from a surface reflection and the normalized radar cross section of the surface,

$$\sigma^0 = \sum_{\text{surf}} \eta[r] \Delta r \cos\phi_0, \tag{A15}$$

where the data is summed over range gates containing surface backscatter.

This result assumes that the received power is sampled sufficiently often to approximate the integrated power with a Riemann sum and that the surface reflection is substantially stronger than any hydrometeor reflections.

APPENDIX B

Derivation of internal and external calibration equations

a. Internal Loopback Calibration

An internal calibration loop provides a way of directly measuring the product of the transmitted power, receiver gain, pulse compression gain (if applicable), and range-weighting function. It consists of an attenuated path from the transmitter to the receiver. A simplified schematic of an internal calibration loop is shown in Fig. 14.

The power measured by the radar during transmission during calibration is an attenuated version of the transmitted waveform. If the loss in the calibration path is l_c the power in watts received during transmit/calibration at range-time r is

$$P_c(r) = P_t g_s \int \frac{\delta(r')}{l_c} |W_s(r'-r)|^2 \partial r'. \tag{B1}$$

where $\delta(r')$ is the Dirac-delta function. This simplifies to

$$P_c(r) = \frac{P_t g_s |W_s(-r)|^2}{l_c}. \tag{B2}$$

With sufficiently dense range gates, the measured power through the calibration loop during transmit is summed to provide an estimator for the product of radar terms, as

$$\sum_{\mathrm{cal}} P_c[r']\Delta r' = \frac{\left\langle P_t g_s \int |W_s(r')|^2 \partial r' \right\rangle}{l_c}. \tag{B3}$$

Substituting the internal calibration terms into the radar equation does not require individual knowledge of the transmit power, receiver gain, pulse compression gain, or range weighting function, as

$$P_\eta(r) = \frac{\left(\sum_{\mathrm{cal}} P_c[r']\Delta r'\right) l_c g^2 \lambda^2 \eta(r)}{(4\pi)^3 r^2 l_{\mathrm{atm}}^2(r) l_{\mathrm{tx}} l_{\mathrm{rx}} l_{\mathrm{rad}}^2} \iint f^4(\theta', \phi') \sin\theta' \partial\theta' \partial\phi' \tag{B4}$$

One source of error with internal loopback calibration systems in addition to measurement error is the coherent phase interaction of the desired calibration signal attenuated through the loopback path (l_c) and the undesired signal that leaks through the isolation of the receiver protection switches (l_{iso}) that turn off the normal receiver path during calibration. If the signal through the receiver protection switches is close in power to that of the calibration signal it will cause a calibration offset. On the other hand, the calibration signal has to be low enough to avoid receiver saturation. Increasing the isolation in the receiver protection network requires additional switches which increases the receiver noise figure. This necessitates a design trade to minimize receiver loss while obtaining a useful calibration signal.

This analysis treats the transmitter and receiver in a steady state with constant transmit power P_t and system gain g_s without either pulse compression gain or range weighting. Depending on the relative phase $\Delta\psi$ between the calibration path and the receiver protection path the calibration power P_c related to the transmitted power is the sum of the two phasers in voltage. The receiver calibration power is

$$P_c = P_t \left(\frac{1}{l_c} + \frac{1}{l_{\mathrm{iso}}} + \frac{2}{\sqrt{l_c l_{\mathrm{iso}}}} \cos(\Delta\psi) \right). \tag{B5}$$

The possible calibration error in decibels associated with this approximation is

$$\Delta\mathrm{Cal} = -10\log_{10}\left(1+\frac{l_c}{l_{\mathrm{iso}}}+2\sqrt{\frac{l_c}{l_{\mathrm{iso}}}}\cos\Delta\psi\right). \tag{B6}$$

The possible (min and max) calibration error caused by the phase interaction between the calibration path and the receiver protection isolation is shown in Fig. B1. With 30 dB more isolation than calibration loss the absolute error from this effect for CRS is limited to 0.28 dB.

While CRS does not use an external point-target calibration, the integration of the internal loopback signal in time is very similar to the integration of the reflection from a small external calibration fixture such as a corner reflector in range. This allows in both cases for direct calibration of the range weighting function with the external target, removing potential sources of error. In addition, integration of the received target over angle with a scanning antenna can (if the target is stationary and the antenna fully mobile) be used to directly estimate the integrated antenna pattern.

b. External calibration

While the internal calibration tracks transmit power, receiver gain, and pulse compression gain very well, CRS uses an ocean surface calibration for absolute measurements as per Li et al. (2005).

The external calibration equation uses the range-integrated surface backscatter combined with the internally calibrated radar equation shown in Eq. (B4). Collecting all the range terms in Eq. (B4) save for the volume reflectivity and using a Riemann sum to approximate integrating over the ranges containing surface backscatter gives

$$\sum_{\mathrm{surf}} P_\eta[r']r'^2 l_{\mathrm{atm}}^2(r')\Delta r' = \sum_{\mathrm{cal}} P_c[r'']\Delta r'' \frac{l_c g^2\lambda^2 \iint f^4(\theta',\phi')\sin\theta'\partial\theta'\partial\phi' \sum_{\mathrm{surf}}\eta(r')\Delta r'}{(4\pi)^3 l_{\mathrm{tx}} l_{\mathrm{rx}} l_{\mathrm{rad}}^2}. \tag{B7}$$

Substituting $\sigma^0/\cos\phi_0$ in place of $\sum_{\mathrm{surf}}\eta[r']\Delta r'$ as per Eq. (20) gives

$$\frac{\sum_{\mathrm{surf}} P_\eta[r']r'^2 l_{\mathrm{atm}}^2(r')\Delta r'}{\sum_{\mathrm{cal}} P_c[r'']\Delta r''} = \frac{l_c g^2\lambda^2 \iint f^4(\theta',\phi')\sin\theta'\partial\theta'\partial\phi'\sigma^0}{(4\pi)^3 l_{\mathrm{tx}} l_{\mathrm{rx}} l_{\mathrm{rad}}^2 \cos\phi_0}. \tag{B8}$$

Collecting all non-radar parameter terms gives a calibration constant C_{ext} in units of m^2,

$$C_{\text{ext}} = \frac{\cos\phi_0 \sum_{\text{surf}} P_\eta[r'] r'^2 l_{\text{atm}}^2(r') \Delta r'}{\sigma^0 \sum_{\text{cal}} P_c[r''] \Delta r''} = l_c \left\langle \frac{g^2 \lambda^2 \iint f^4(\theta', \phi') \sin\theta' \partial\theta' \partial\phi'}{(4\pi)^3 l_{\text{tx}} l_{\text{rx}} l_{\text{rad}}^2} \right\rangle. \tag{B9}$$

The external calibration constant C_{ext} is calculated during calibration maneuvers using estimates of surface backscatter and atmospheric attenuation. For the IMPACTS 2020 field campaign, external coefficients were calculated during three calibration maneuvers at 8 degrees off nadir to reduce the impact of wind on σ_0.

Substituting the external calibration constant C_{ext} derived from the ocean surface calibration into the internal calibration Eq. (B4) and solving for volume reflectivity gives a significantly simplified internally-calibrated radar equation,

$$\hat{\eta}[r] = \frac{P_\eta r^2 l_{\text{atm}}^2(r)}{C_{\text{ext}} \sum_{\text{cal}} P_c[r'] \Delta r'}. \tag{B10}$$

This calibrated volume reflectivity estimator uses the external calibration coefficient constant to provide the absolute power to volume reflectivity conversion combined with the internal calibration signal to provide continuous tracking of changes in the transmitter and receiver gain.

References

Barros, A., and Coauthors, 2014: NASA GPM-ground validation: Integrated precipitation and hydrology experiment 2014 science plan.

Bringi, V., and V. Chandrasekar, 2001: *Polarimetric Doppler weather radar: principles and applications*. Cambridge University Press.

Caylor, I., G. Heymsfield, R. Meneghini, and L. Miller, 1997: Correction of sampling errors in ocean surface cross-sectional estimates from nadir-looking weather radar. *Journal of Atmospheric and Oceanic Technology*, **14 (1)**, 203–210.

Doviak, R. J., and D. S. Zrnić, 2006: *Doppler radar and weather observations*. Courier Corporation.

Evans, K. F., J. R. Wang, P. E. Racette, G. Heymsfield, and L. Li, 2005: Ice cloud retrievals and analysis with the compact scanning submillimeter imaging radiometer and the cloud radar system during crystal face. *Journal of Applied Meteorology*, **44 (6)**, 839–859.

Fukao, S., K. Hamazu, and R. J. Doviak, 2014: *Radar for meteorological and atmospheric observations*. Springer.

Hand, T., and Coauthors, 2013: Dual-band shared aperture reflector/reflectarray antenna: Designs, technologies and demonstrations for NASA's ACE radar. *2013 IEEE International Symposium on Phased Array Systems and Technology*, IEEE, 352–358.

Holleman, I., and H. Beekhuis, 2003: Analysis and correction of dual PRF velocity data. *Journal of Atmospheric and Oceanic Technology*, **20 (4)**, 443–453.

Joe, P., and P. May, 2003: Correction of dual prf velocity errors for operational doppler weather radars. *Journal of Atmospheric and Oceanic Technology*, **20 (4)**, 429–442.

Kozu, T., 1995: A generalized surface echo radar equation for down-looking pencil beam radar. *IEICE Transactions on Communications*, **78 (8)**, 1245–1248.

Li, L., G. M. Heymsfield, P. E. Racette, L. Tian, and E. Zenker, 2004: A 94-GHz Cloud Radar System on a NASA high-altitude ER-2 aircraft. *Journal of Atmospheric and Oceanic Technology*, **21 (9)**, 1378–1388.

Li, L., G. M. Heymsfield, L. Tian, and P. E. Racette, 2005: Measurements of ocean surface backscattering using an airborne 94-GHz cloud radar-implication for calibration of airborne and spaceborne W-band radars. *Journal of Atmospheric and Oceanic Technology*, **22 (7)**, 1033–1045.

Li, L., and Coauthors, 2016: The NASA High-altitude Imaging Wind and Rain Airborne Profiler (HIWRAP). *IEEE Trans. Geosci. Remote Sens.*, **54 (1)**, 298–310.

Long, M. W., 2001: *Radar Reflectivity of Land and Sea, Third Edition*. Artech House.

Mace, G. G., Q. Zhang, M. Vaughan, R. Marchand, G. Stephens, C. Trepte, and D. Winker, 2009: A description of hydrometeor layer occurrence statistics derived from the first year of merged cloudsat and calipso data. *Journal of Geophysical Research: Atmospheres*, **114 (D8)**.

Majurec, N., S. Sekelsky, S. Frasier, and S. Rutledge, 2004: The Advanced Multi-Frequency Radar (AMFR) for remote sensing of clouds and precipitation. *32nd Conf. Radar Meteorology, Albuquerque, NM*.

McLinden, M. L., J. Carswell, L. Li, G. Heymsfield, A. Emory, J. Cervantes, L. Tian, and Coauthors, 2013: Utilizing versatile transmission waveforms to mitigate pulse-compression range sidelobes with the hiwrap radar. *Geoscience and Remote Sensing Letters, IEEE*, **10 (6)**, 1365–1368.

McLinden, M. L., E. J. Wollack, G. M. Heymsfield, and L. Li, 2015: Reduced image aliasing with microwave radiometers and weather radar through windowed spatial averaging. *Geoscience and Remote Sensing, IEEE Transactions on*, **53 (12)**, 6639–6649.

NASA/DFRC, 2002: ER-2 airborne laboratory experimenter handbook. Tech. rep., NASA Dryden Flight Research Center. URL https://www.nasa.gov/sites/default/files/189893main_ER-2_handbook_02.pdf.

Probert-Jones, J., 1962: The radar equation in meteorology. *Quarterly Journal of the Royal Meteorological Society*, **88 (378)**, 485–495.

Rincon, R. F., T. Fatoyinbo, B. Osmanoglu, S. Lee, K. J. Ranson, G. Sun, M. Perrine, and C. Du Toit, 2015: Ecosar: P-band digital beamforming polarimetric and single pass interferometric sar. *2015 IEEE Radar Conference (RadarCon)*, IEEE, 0699–0703.

Stephens, G. L., S.-C. Tsay, P. W. Stackhouse Jr, and P. J. Flatau, 1990: The relevance of the microphysical and radiative properties of cirrus clouds to climate and climatic feedback. *Journal of the atmospheric sciences*, **47 (14)**, 1742–1754.

Stephens, G. L., and Coauthors, 2002: The cloudsat mission and the a-train: A new dimension of space-based observations of clouds and precipitation. *Bulletin of the American Meteorological Society*, **83 (12)**, 1771–1790.

Stephens, G. L., and Coauthors, 2008: CloudSat mission: Performance and early science after the first year of operation. *Journal of Geophysical Research: Atmospheres*, **113 (D8)**.

Tanelli, S., S. L. Durden, E. Im, K. S. Pak, D. G. Reinke, P. Partain, J. M. Haynes, and R. T. Marchand, 2008: CloudSat's Cloud Profiling Radar after two years in orbit: Performance, calibration, and processing. *Geoscience and Remote Sensing, IEEE Transactions on*, **46 (11)**, 3560–3573.

Toon, O. B., and Coauthors, 2010: Planning, implementation, and first results of the tropical composition, cloud and climate coupling experiment (tc4). *Journal of Geophysical Research: Atmospheres*, **115 (D10)**.

Torres, S. M., Y. F. Dubel, and D. S. Zrnić, 2004: Design, implementation, and demonstration of a staggered prt algorithm for the wsr-88d. *Journal of Atmospheric and Oceanic Technology*, **21 (9)**, 1389–1399.

Vivekanandan, J., and Coauthors, 2015: A wing pod-based millimeter wavelength airborne cloud radar. *Geoscientific Instrumentation, Methods and Data Systems*, **4 (2)**, 161–176.

LIST OF TABLES

TABLE 1. Performance metrics of the solid-state Cloud Radar System

Frequency	94.0 GHz
Transmitter Type	Solid-State Power Amplifier
Peak Transmitter Power	30 Watts
Antenna Type	Reflectarray
Antenna Gain	51 dB
Antenna Beamwidth	0.45 degrees
Vertical Resolution	115 m
Vertical Sampling	26.25 m
Approx. Horizontal Resolution	125 m
Approx. Horizontal Sampling	50 m
Pulse Repetition Interval	224/280 μs (staggered)
Sensitivity	-30 dBZe (10 km, 0.5s integration time)

LIST OF FIGURES

(a)

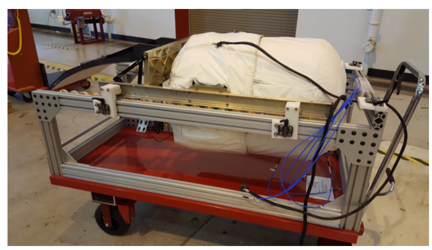

(b)

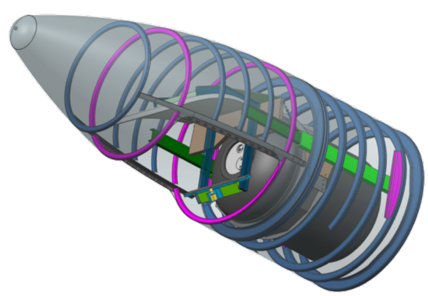

(c)

FIG. 1. CRS flies in the aft and midbody section of either ER-2 superpod. The antenna points through an open window, eliminating radome loss. The RF electronics are located in the aft section of the superpod, and the digital subsystems are located in the superpod midbody. (a) The NASA ER-2 superpod and ER-2 window. (b) A photograph of the pressurized CRS RF subsystem prior to installation on the ER-2. (c) An illustration of CRS mounted in the ER-2 superpod.

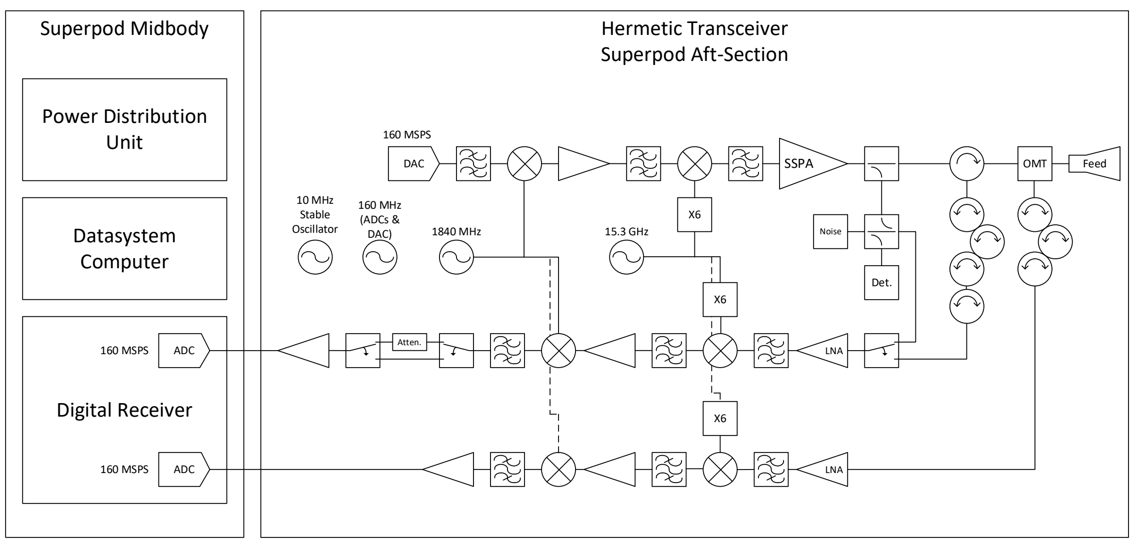

744 Fig. 2. Simplified CRS Block Diagram. The RF and IF subsystems, as well as waveform generation and
745 control are contained within a pressurized canister in the aft section of the ER-2 superpod. Power distribution,
746 the digital receiver, and the data system are located in the mid-body of the ER-2 superpod.

FIG. 3. The 30 W 94 GHz GaAs solid state power amplifier.

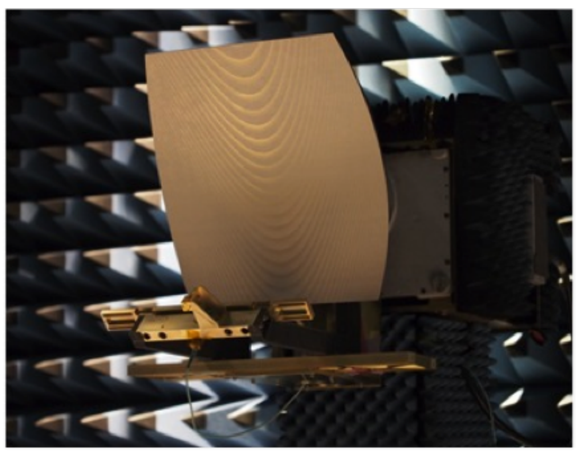

FIG. 4. The CRS reflectarray antenna during anechoic chamber testing

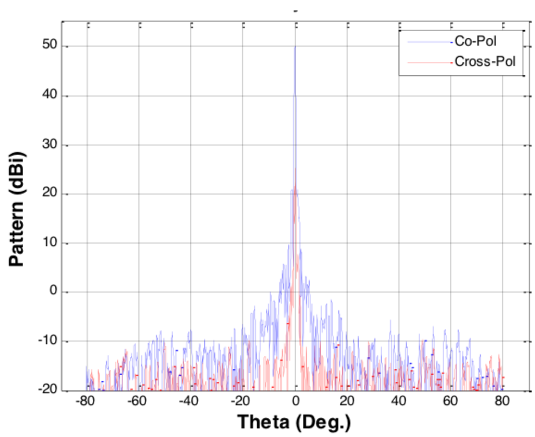

(a)

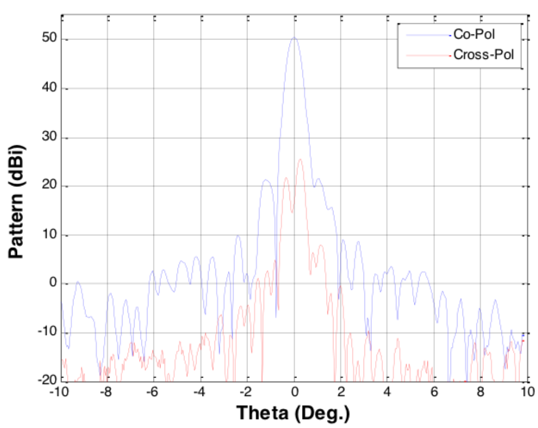

(b)

FIG. 5. The CRS reflectarray antenna pattern. (a) Full antenna pattern. (b) Antenna pattern from -10 to 10 degrees.

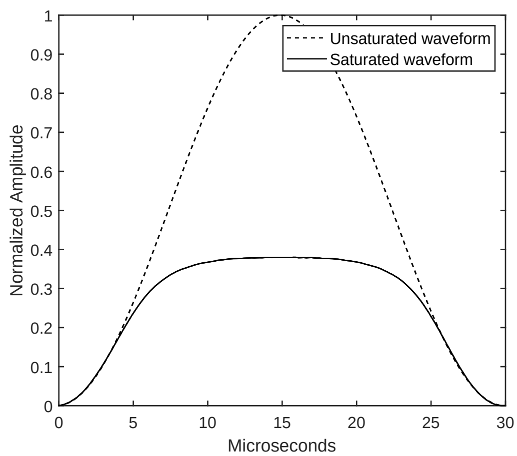

FIG. 6. The relative amplitude of the CRS chirp before (dashed) and after (solid) transmitter saturation. While the waveform generator produces a Hann taper, transmitter saturation reduces the taper substantially.

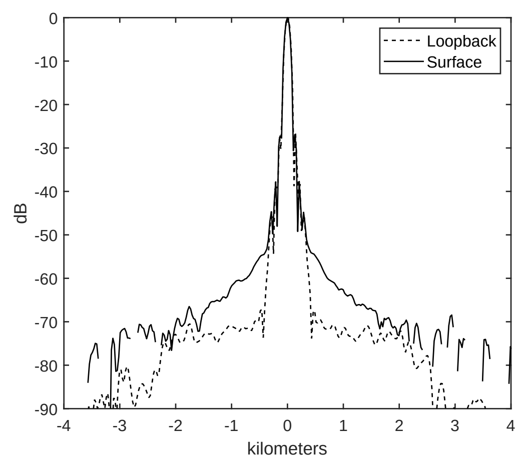

FIG. 7. The pulse compressed chirp showing sidelobes from internal calibration data (dashed) and from an exceptionally strong surface echo (solid).

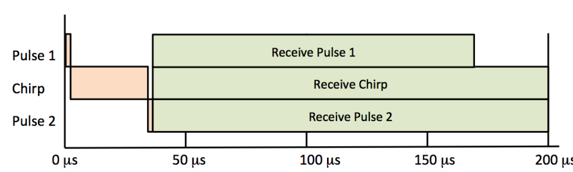

FIG. 8. Illustration of the CRS Frequency Diversity Waveform. Two pulses and a chirp are transmitted in a train at slightly offset frequencies, then all three frequencies are received simultaneously. This waveform is repeated at an alternating 224 μs, 280 μs pulse repetition interval.

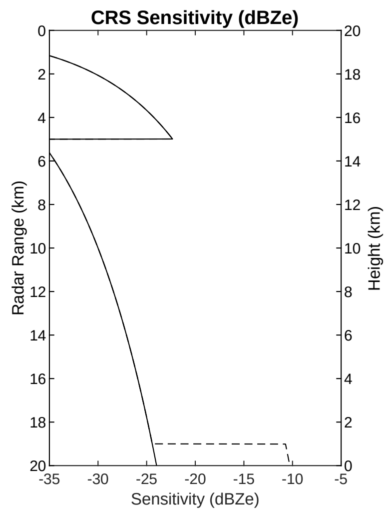

FIG. 9. Approximate sensitivity of CRS with radar range and height assuming a 20 km cruising ER-2 altitude. Sensitivity between 5 km from the aircraft and 1 km from the surface is improved by 14 dB with pulse compression. Pulsed CW data (dashed) may be used near the surface in the presence of strong pulse compression range sidelobes.

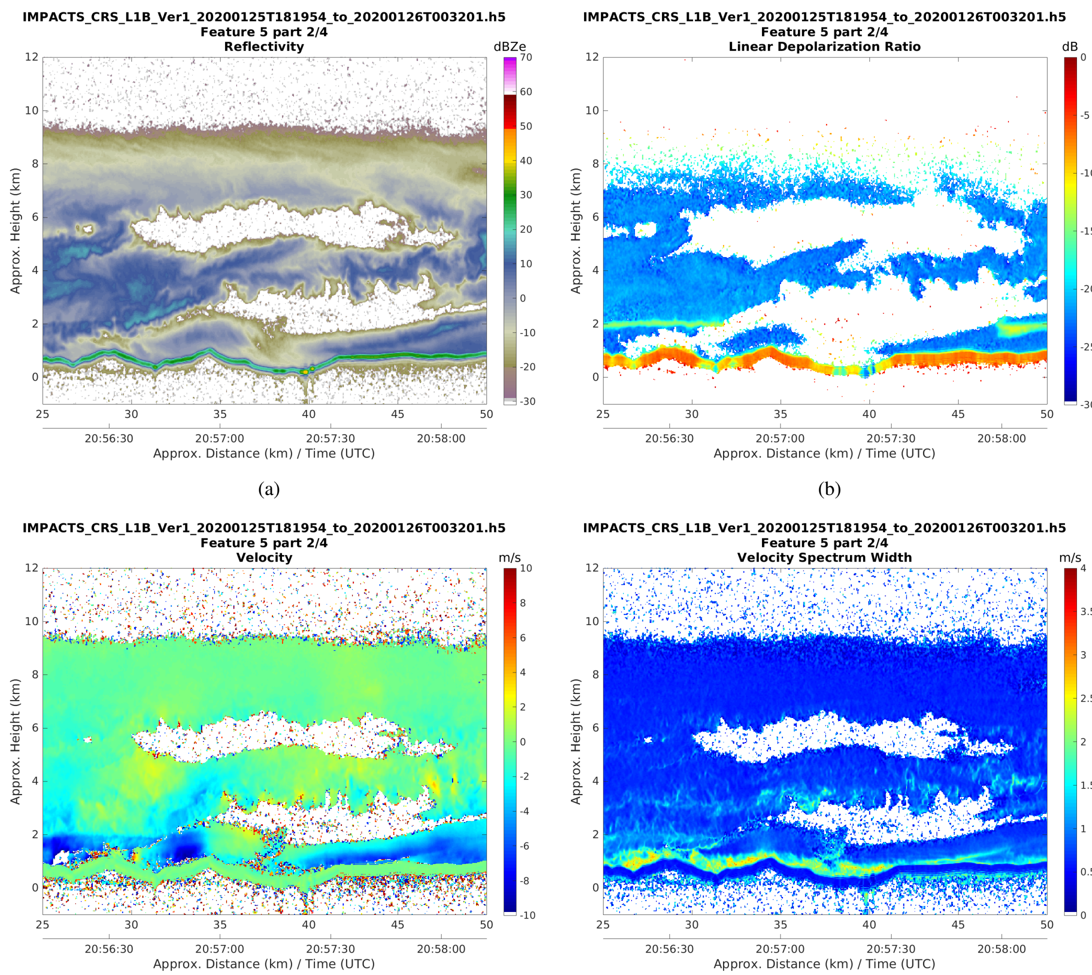

FIG. 10. Example data products from the Version 1 data release, January 25, 2020 science flight for the IMPACTS field campaign using Chirped data only. The horizontal axis in each subplot is along-track distance and time, and the vertical axis is the approximate height above sea level. (a) Radar reflectivity without estimated attenuation correction. (b) Linear Depolarization Ratio. (c) Doppler Velocity (m/s) with the relative aircraft motion subtracted. Positive values are upward velocity and negative values are downward. (d) Doppler velocity spectrum width including the effects of aircraft motion.

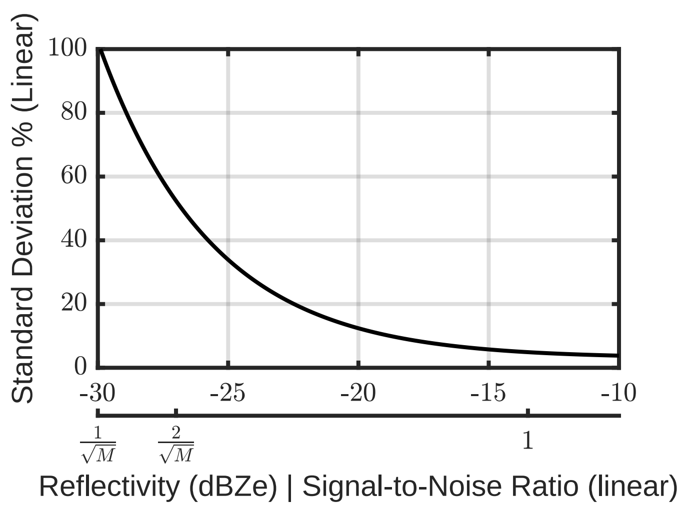

FIG. 11. Expected standard deviation of CRS reflectivity measurements at 10 km range as a percentage of the reflectivity, assuming a sensitivity of -30 dBZe and a spectrum width of 1 m/s.

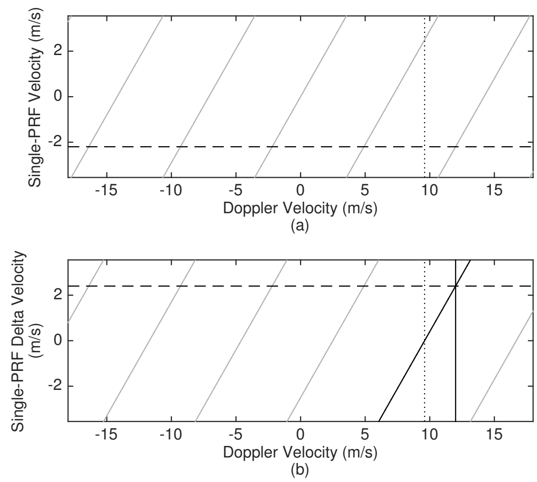

FIG. 12. Example of the CRS Dual-PRF Doppler Algorithm. (a) A single-PRF velocity estimate (horizontal dashed line) and an initial dual-PRF estimate using Eq. (16) (vertical dotted line) with the single-PRF velocity ambiguity illustrated by the light grey lines. The single-PRF velocity is ambiguous, possibly falling on any intersection of the horizontal and diagonal lines. (b) The single-PRF velocity difference (ΔV) from Eq. (17) (horizontal dashed line) and the initial dual-PRF estimate (vertical dotted line). The final velocity estimate is the vertical solid line. The bolded diagonal line shows the single-PRF Nyquist interval shifted to the initial dual-PRF estimate. This highlights the resistance of the algorithm to unaliasing errors as the single-PRF Nyquist interval (bold) is centered on the initial dual-PRF estimate.

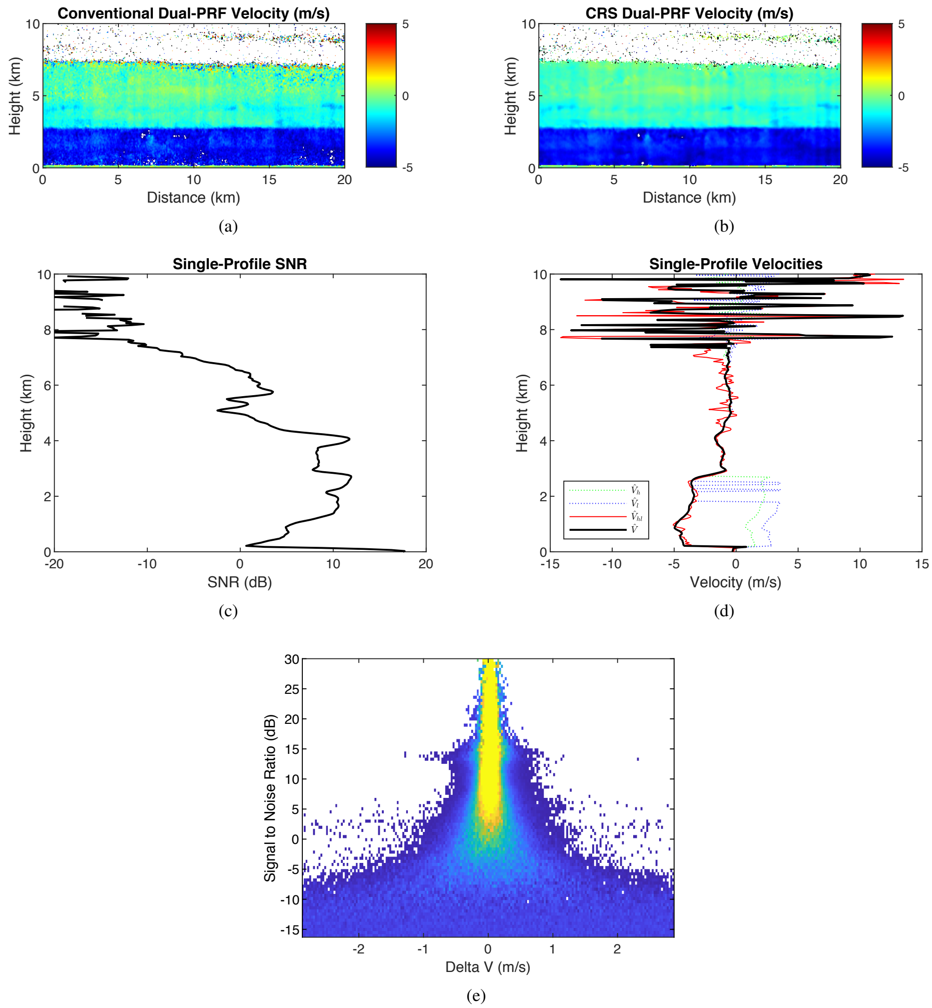

FIG. 13. Doppler data example demonstrating the CRS unfolding algorithm. (a) Conventional dual-PRF velocity image from Eq. (16). The horizontal axis is along-track distance. The vertical axis is height above sea level. The color scale is Doppler velocity in m/s, with a negative velocity indicating downward motion. (b) Dual-PRF data with the CRS algorithm from Eq. (18), visually showing reduced noise compared to the conventional algorithm. (c) The SNR of a single vertical radar profile. (d) Velocity estimates of a single vertical radar profile. The dashed lines are single-PRF velocities, folding in the rain layer below 3 km. The solid red line is the dual-PRF velocity from Eq. (16), showing a larger standard deviation but not folding due to the larger Nyquist velocity. The solid black line is the CRS dual-PRF velocity algorithm with both the expanded Nyquist velocity and reduced uncertainty. (c) Heat map of the velocity correction term from Eq. (17) (horizontal) with the received power SNR (vertical). The algorithm is resistant to folding errors for SNR > -7 dB as used on CRS.

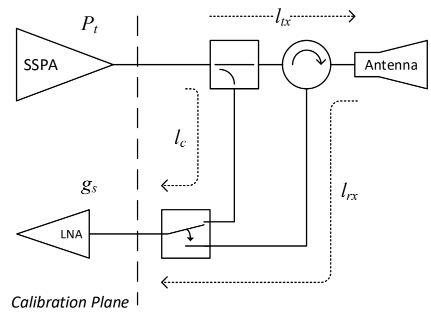

786 FIG. 14. Simplified schematic of the CRS internal calibration loop. The transmitted power P_t is coupled through into the radar receiver with gain g_s. The calibration path loss is l_c. All radar parameters are calibrated with the exception of the transmit loss (l_{tx}), antenna, and receiver loss prior to the calibration switch (l_{rx}).

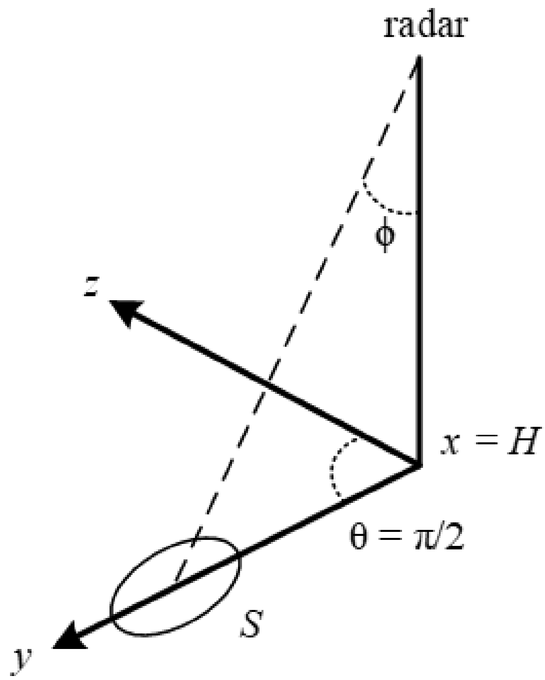

Fig. A1. Radar coordinate system. The radar lies at the origin of both the spherical and cartesian coordinates. The region illuminated by the antenna is labeled *S*, however a uniform illumination over this region is not assumed.

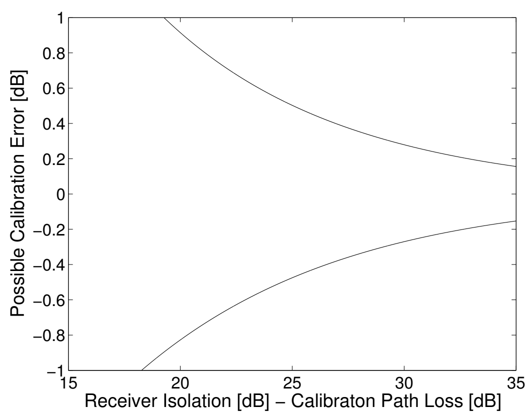

Fig. B1. Possible calibration error in decibels introduced by the coherence of the calibration path with that of the receiver protection switch path. The CRS receiver protection isolation is more than 30 dB higher than the calibration path loss.